Mott transition controlled by lattice-orbital coupling in 3d-metal-doped double-layer ruthenates

J. Peng, M. Q. Gu, X. M. Gu, G. T. Zhou, X. Y. Gao, J. Y. Liu, W. F. Xu, G. Q. Liu, X. Ke, L. Zhang, H. Han, Z. Qu, D. W. Fu, H. L. Cai, F. M. Zhang, Z. Q. Mao, and X. S. Wu

Phys. Rev. B **96**, 205105 — Published 2 November 2017

DOI: 10.1103/PhysRevB.96.205105

Mott transition controlled by lattice-orbital coupling in 3*d*-metal-doped double layer ruthenates

J. Peng,[1,2] M. Q. Gu,[1] X. M. Gu,[1] G. T. Zhou,[1] X. Y. Gao,[1] J. Y. Liu,[2] W. F. Xu,[2] G. Q. Liu,[3*] X. Ke,[4] L. Zhang,[5] H. Han,[5] Z. Qu,[5] D. W. Fu,[6] H. L. Cai,[1] F. M. Zhang,[1] Z. Q. Mao,[2†] and X. S. Wu[1‡]

1. *Collaborative Innovation Center of Advanced Microstructures, Laboratory of Solid State Microstructures, School of Physics, Nanjing University, Nanjing 210093, China*
2. *Department of Physics and Engineering Physics, Tulane University, New Orleans, LA 70118, USA*
3. *Ningbo Institute of Material Technology and Engineering, Chinese Academy of Sciences, Ningbo 315201, China*
4. *Michigan State University, East Lansing, MI 48825, USA*
5. *High Magnetic Field Laboratory, Chinese Academy of Sciences, Hefei, 230031, China*
6. *Ordered Matter Science Research Center, Southeast University, Nanjing, 211189,China*

We have investigated unusual phase transitions that were triggered by chemical doping in $Ca_3Ru_2O_7$. Our experiments showed that doping with a few percent of Mn (>4%) can change the quasi-two-dimensional metallic state of $Ca_3Ru_2O_7$ into a Mott insulating state with a G-type antiferromagnetic order, but this Mott state cannot be induced by Fe doping. By combining these results with first-principles calculations, we show that lattice-orbital coupling (LOC) plays an important role in the Mott transition. Interestingly, the transition temperature T_{MIT} is found to be predetermined by a structural parameter denoted by $c/\sqrt{ab}$ at temperatures far above *N*éel temperature T_{N}. This LOC-assisted Mott transition clearly contrasts with the band-filling picture. It is addressed that this type of Mott transition originates in the strong scattering centers formed by specific 3*d*-dopants. The dopant-scattering picture is then applied to explain the puzzling doping effects that occur in other ruthenates and 3*d*-oxides. Our findings will advance the general understanding of how the unusual properties of 4*d* correlated systems are governed by the complex interplay that occurs among the charge, spin, lattice and orbital degrees of freedom.

*liugq@nimte.ac.cn

†zmao@tulane.edu

‡xswu@nju.edu.cn

I. INTRODUCTION

Complex interplay among the charge, orbital, lattice and spin degrees of freedom is believed to underlie the broad range of fascinating phenomena that occur in strongly correlated systems [1]. An appropriate corollary to this interplay is the tunability of magnetic and electronic phases based on the use of nonthermal parameters such as chemical doping, pressure, or magnetic fields that is exemplified in high-temperature (high-T_c) superconductive cuprates [2-4] and colossal magnetoresistive manganites [5-8]. Comprehension of these complex phase transitions requires the constitutive relations among the different degrees of freedom to be determined but an appropriate solution remains elusive.

Ruddlesden-Popper (RP)-type layered ruthenates of the form $A_{n+1}Ru_nO_{3n+1}$ are typical strongly correlated materials with a rich variety of different properties, including spin-triplet superconductivity in Sr_2RuO_4, a field-tuned electronic nematic phase in $Sr_3Ru_2O_7$, itinerant ferromagnetism in $SrRuO_3$ [9-13], an antiferromagnetic (AFM) Mott insulating state in Ca_2RuO_4, and paramagnetic (PM) 'bad' metallicity in $CaRuO_3$ [13,14]. The larger radial extension of the Ru 4*d* orbitals when compared with the 3*d* orbitals in 3*d* correlated systems such as cuprates and manganites leads to weaker electron correlations and stronger orbital-lattice coupling that make these ruthenate systems more sensitive to external stimuli, such as chemical doping, magnetic fields, and applied pressure. For example, previous studies showed that some 3*d* ions have similar ionic radii to that of Ru^{4+} and can thus be easily incorporated into the crystal structure. A tiny amount of Ti substitution for Ru in Sr_2RuO_4 (5%), $Sr_3Ru_2O_7$ (5%), and $Ca_3Ru_2O_7$ (3%), or similar concentrations for Mn substitution in Ru sites in Sr_2RuO_4 (3%) and $Sr_3Ru_2O_7$ (5%) is effective for tuning of the electronic/magnetic states from a PM or nearly ferromagnetic (FM) metallic state to an AFM insulating state [15-23]. In contrast, doping with certain other magnetic 3*d* ions, such as Cr, Co, and Fe, preserves the metallic electronic states of pristine compounds and results in a tendency towards FM ordering in $SrRuO_3$, $CaRuO_3$ and Sr_2RuO_4 [15,24-26].

In this paper, we focus on the mechanism of a Mott transition that is triggered by a tiny amount of chemical doping of the double-layered ruthenate $Ca_3Ru_2O_7$. $Ca_3Ru_2O_7$ has very rich physical properties, with spins that are ordered antiferromagnetically at a *N*éel temperature T_N of 56 K [27]. This AFM state is characterized by FM RuO_2 bilayers that are coupled antiferromagnetically along the *c*-axis with spins pointing along the *a*-axis [28,29]. A first-order metal-insulator transition (MIT) that is accompanied by a change in the spin direction from along the *a*-axis to along the *b*-axis occurs at T_{MIT} = 48 K [28,29]. These two magnetic states were named as AFM-a and AFM-b, respectively [29]. This MIT is followed by quasi-2D metallic transport behavior at T<30 K in floating-zone-grown single crystals [30]. Angle-resolved photoemission spectroscopy measurements have shown that this metallicity below 30 K originates from a very small ungapped section of the Fermi surface that survived through the MIT [31]. Theoretical studies indicate that the anisotropic gap opening at 48 K is induced by interplay between the spin-orbit (SO) coupling and Coulomb repulsion [32]. Our previous work showed that the electronic and magnetic ground states of $Ca_3Ru_2O_7$ are extremely sensitive to chemical doping; Ti doping of as low as 3% can tune the system from a quasi-2D metallic state with AFM-b order to a Mott insulating state with a nearest neighbor G-type AFM order (G-AFM) [22,23]. Schematic diagrams of the AFM-b and G-AFM magnetic structures are shown in Figure 1b. Additionally, this Mott insulating state can be suppressed by application of a moderate magnetic field (~8 T) or low hydrostatic pressure (~0.04 GPa) [33,34], and this produces complex phase diagrams. All these observations indicate the existence of competing physical interactions with similar magnitudes, such as those of SO coupling, kinetic energy, Coulomb repulsion, exchange interactions, and the crystal field. Understanding these complex competing interactions is clearly challenging but lies at the heart of strongly correlated material physics.

The aims of this paper are two-fold. First, we intend to demonstrate that the doping effects of magnetic Mn ions are dissimilar to those of other magnetic ions, such as Cr, Fe, Co and Ni, but are unexpectedly similar to those of the nonmagnetic Ti ion. Second, we aim to address the question of why nonmagnetic Ti and magnetic Mn doping can induce Mott transitions, while these transitions are not induced by other 3*d* dopants. Through a comparison of the experimental and theoretical results, we find that the Mott transitions that are induced by very low concentration Mn or Ti doping in $Ca_3Ru_2O_7$ cannot be simply classified as band-filling- or band-width-controlled Mott transitions, but are in fact tuned by the lattice-orbital coupling LOC. We disclosed that these Mott transitions originate in the local electronic configurations of specific dopants, and that this dopant selectivity is universal in transition metal oxides (TMOs).

II. EXPERIMENTAL PHASE DIAGRAM OF MAGNETIC AND ELECTRONIC PROPERTIES

Concentration-dependent electronic and magnetic phase diagrams of $Ca_3(Ru_{1-x}Mn_x)_2O_7$ and $Ca_3(Ru_{1-x}Fe_x)_2O_7$ have been established based on transport, magnetic and neutron scattering measurements. The phase diagram for $Ca_3(Ru_{1-x}Mn_x)_2O_7$ is shown on the right side of Fig. 1a. Several distinct ordered magnetic phases can be observed in this diagram. The end member (at x=0) first shows an AFM transition at 56 K, which is then followed by MIT at 48 K, as noted above. When the Mn doping level is in the $0 < x(\mathrm{Mn}) \leqslant 0.04$ range, the temperature range of AFM-a phase is broadened. Additionally, an intermediate magnetic (IM) phase also emerges in a narrow temperature range that lies immediately below T_{MIT}. These features were clearly revealed by the results of magnetic susceptibility and resistivity measurements of the samples in this composition region [35].

When $x(\mathrm{Mn}) > 0.04$, the multiple magnetic transitions merge into a single transition. We present magnetic susceptibility data for the 5% Mn-doped sample in Fig. 2a, where a single transition located near $T_N = 62$ K is clearly shown in the susceptibility characteristic for field applied along both the *a*- and *b*-axes. Elastic neutron scattering measurements performed on this 5% Mn-doped sample proved that the magnetic state below 62 K is characterized by a G-AFM order. Fig. 2a also presents the intensity of the magnetic diffraction peak at (1 0 2) as a function of temperature, which shows a dramatic increase when the temperature is reduced below the magnetic transition temperature (62 K) and quickly becomes saturated.

The left side of Fig. 1a shows the doping effects of the Fe ions. Fe substitution for Ru effectively broadens the temperature range of the AFM-a state, but does not induce an insulating G-AFM state. We present susceptibility data for the 5% Fe-doped sample in Fig. 2b, which demonstrate that the Fe doping increases T_N but reduces T_{MIT}. Elastic neutron scattering measurements of the 5% Fe-doped $Ca_3Ru_2O_7$ sample showed that the magnetic ground state does not evolve into the G-AFM state that was observed in the 5% Mn-doped sample. Instead, the results indicate the coexistence of the AFM-b phase and an incommensurate phase that is characterized by a cycloidal spiral spin structure [36]. It should also be mentioned that an IM phase emerges within a narrow temperature range that occurs immediately below T_{MIT} for compositions with $0 < x(\mathrm{Fe}) < 0.04$. These features are clearly shown by the results of the magnetic susceptibility and resistivity measurements of the samples in this composition regime [37].

Our transport measurements indicated that Mn doping (>4%) also induces a dramatic electronic state change that occurs concomitantly with the magnetic ground state transition from AFM-b to G-AFM. For the G-AFM state (where $x(\mathrm{Mn}) \geq 0.05$), ρ_{ab} increases by several orders of magnitude, thus indicating a truly insulating state. For the $0 < x(\mathrm{Mn}) \leqslant 0.04$ range, in which multiple magnetic transitions are observed, the AFM-a phase remains metallic, whereas the AFM-b phase shows localized behavior at temperatures down to 2 K (Fig. 2c); This is distinct from the quasi-2D metallic behavior below 30 K observed in pure $Ca_3Ru_2O_7$ synthesized by the floating-zone-grown method. However, the amplitude of the metal-to-localized state transition in this composition range is comparable with that of pristine $Ca_3Ru_2O_7$.

The transport behavior of Fe-doped $Ca_3Ru_2O_7$ is shown in Fig. 2d. ρ_{ab} maintains metallic behavior for the AFM-a phase ($T_{MIT}<T<T_N$) but demonstrates localized behavior for the AFM-b phase ($T<T_{MIT}$); it does not evolve into the insulating state that was observed in the Mn-doped samples. When the Fe concentration is less than 3%, the AFM-b phase maintains metallic behavior at temperatures well below T_{MIT}.

The doping effects of the Fe and Mn ions in $Ca_3Ru_2O_7$ are compared with the corresponding effects of Ti and Cr ions that were previously reported. With Ti doping, the system evolves from a quasi-2D metal state with an AFM-b magnetic structure into a weakly localized state for $0 < x < 0.03$, and then finally into a Mott insulator state with G-AFM order for $x \geq 0.03$. For $0 < x \leq 0.03$, the system shows complex magnetic transitions with an IM phase in a narrow temperature range between AFM-a and AFM-b [22,23]. The Cr doping in $Ca_3Ru_2O_7$ leads to expansion of the AFM-a metallic state ($T_{MIT} < T < T_N$) temperature range and also preserves the AFM-b magnetic state for $T < T_{MIT}$ [38].

Other 3*d* ions such as Co, Ni and Cu show similar doping effects to those of Fe and Cr. The jump amplitudes of ρ_{ab} at T_{MIT} for 5% Co-, Ni- and Cu-doped $Ca_3Ru_2O_7$ samples are approximately the same size as that of pristine $Ca_3Ru_2O_7$ and the 5% Fe-doped sample (see Fig. 3a). Additionally, the two cusps in the temperature-dependent magnetic susceptibility ($\chi(T)$) characteristics for $Ca_3Ru_2O_7$ that correspond to T_N and T_{MIT} were also observed in the 5% Fe- and Ni-doped samples (see Fig. 3b). Comparisons between the phase diagrams of $Ca_3(Ru_{1-x}Mn_x)_2O_7$ and $Ca_3(Ru_{1-x}Fe_x)_2O_7$ with previously reported diagrams for $Ca_3(Ru_{1-x}Ti_x)_2O_7$ and $Ca_3(Ru_{1-x}Cr_x)_2O_7$, as well as the magnetic and transport measurements of $Ca_3Ru_2O_7$ when doped with other 3*d* ions, demonstrate that the doping effects of Mn are similar to those of Ti ions but remain distinct from those of other 3*d* ions.

III. THEORETICAL UNDERSTANDING OF THE PHASE DIAGRAM

A Mott transition with a G-AFM ground state was previously observed in the single-layered ruthenate Ca_2RuO_4 at temperatures below 110 K [39]. Theoretical studies showed that this Mott transition is inherently related to distortion of the RuO_6 octahedron [40,41]. To understand the Mott transition that is caused by Ru-site doping in $Ca_3Ru_2O_7$, we studied the temperature dependence of the crystal structure of both the 9% Mn- and 5% Fe-doped samples, which feature a Mott insulating state with G-AFM order and a localized state with an AFM-b order, respectively (see Fig. 1). The temperature dependences of the lattice parameters *a*, *b* and *c* with error bars for both samples are shown in Fig. 4a. In the 9%-Mn doped sample, the *c*-axis is shortened by ~0.52% below T_N (= T_{MIT}) and the *b*-axis is elongated accordingly by ~0.75%; simultaneously, the *a*-axis remains almost unchanged across the phase transition, which suggests flattening of the RuO_6 octahedron below the phase transition temperature. The magnitudes of the lattice parameter changes in the Mn-doped sample are comparable to those that were observed in the Ti-doped sample across T_{MIT} (where the changes in b and c in the 3% Ti-doped sample were approximately +1.1% and −0.85%, respectively [23]). However, no remarkable structural distortions were observed in the 5% Fe-doped sample at the phase transition from AFM-a to the AFM-b+IC state (46 K) [36]. This indicates that the magnetic phases are intrinsically related to the crystal's structural distortions.

To understand the relationship between the structural and magnetic transitions, we performed Local-density approximation (LDA) + static U calculations for $Ca_3Ru_2O_7$. In Ti-doped $Ca_3Ru_2O_7$, it was previously demonstrated that a moderate U of 2 eV is necessary to reproduce the experimental band gap for the G-AFM phase [33]. Figure 4b presents the dependences of the total energies on the parameter $c/\sqrt{ab}$ for the two distinct magnetic structures (i.e., AFM-a/b and G-AFM). In the calculations, the crystal volume is kept constant. The minima of the two lines indicate the points at which these two phases can be stabilized. Figure 4b clearly shows that the stabilization of the G-AFM phase corresponds to a smaller $c/\sqrt{ab}$ when compared with that of the AFM-a/b phase. We selected several compositions (5% Fe-, 3% Ti-, 10% Ti- and 9% Mn-doped $Ca_3Ru_2O_7$, along with the pristine compound) that have AFM-a/b or G-AFM phases. The $c/\sqrt{ab}$ values of these compositions, which were derived from neutron or X-ray diffraction measurements, are placed at the corresponding positions along the horizontal axis in Fig. 4b. The three lines on the right, which correspond to the compounds with the AFM-a/b ground state, show larger $c/\sqrt{ab}$ values, while the compounds with insulating G-AFM ground states have smaller $c/\sqrt{ab}$ values. Our calculations reflect the relationship between the magnetic phase transition and the structural deformation. Sudden flattening of the crystal lattice was observed at the ordering temperature of the G-AFM phase. In contrast, no octahedral flattening was probed in the Fe-doped samples, which show an AFM-b ground state.

Within an octahedral crystal field, the Ru^{4+} 4*d* orbital splits into high energy e_g orbitals and low energy t_{2g} orbitals, as shown in Fig. 5(a). Because of the large splitting energy between e_g and t_{2g} in the 4*d* orbitals, all four of the 4*d* electrons of Ru^{4+} prefer to fill the low energy t_{2g} orbitals. Flattening of the RuO_6 octahedron will split the t_{2g} orbitals further into the singly-degenerate *xy* orbital and doubly-degenerate *xz/yz* orbitals. The downward-shifted *xy* orbital is then more energetically favored than the *xz/yz* orbitals. When the spin polarization is taken into consideration, the band structure of the doped $Ca_3Ru_2O_7$ is calculated using the LDA+U method. The projected density of states (PDOS) for the Ru t_{2g} bands (d_{xy} and d_{xz}/d_{yz}) is calculated for the G-AFM state using the experimental structure of the 9% Mn-doped sample. $c/\sqrt{ab}$ is adopted as the tuning parameter as per the calculated magnetic phase diagram.

For larger $c/\sqrt{ab}$ values (Fig. 5b, left side), the spin-up channel is fully occupied for both the *xy* and *xz/yz* orbitals, whereas the spin-down channel is partly occupied, and this results in a finite density of states at the Fermi surface. However, for a smaller $c/\sqrt{ab}$ value (Fig. 5b, right side), the spin-up channel is still fully occupied for both the *xy* and *xz/yz* orbitals. The spin-down channel of the *xy* orbital changes from partly occupied to nearly fully occupied, but the spin-down channel of the *xz/yz* orbitals changes from partly occupied to nearly empty, which indicates an electronic configuration of *xy*(↑↓) *xz/yz*(↑,↑). The gap is opened because of the competition between and the cooperation of the two splittings, i.e., the orbital splitting between the *xy* and *xz/yz* orbitals and the exchange splitting between the spin-up and spin-down channels. Continuous tuning of the parameter $c/\sqrt{ab}$ (Fig. 5c) causes the gap value to increase monotonically with decreasing $c/\sqrt{ab}$, and this is accompanied by charge transfer from the *xz/yz* orbital to the *xy* orbital, as illustrated by the systematic variation of the orbital occupancy numbers n_{xy} and $n_{xz/yz}$ in Fig. 5c. LDA+U calculations can successfully explain the Mott transition in this series. The sudden flattening of the RuO_6 octahedron at T_N (= T_{MIT}) stabilizes the nearest neighbor AFM structure (G-AFM), thus causing charge transfer from the *xz/yz* orbital to the *xy* orbital and polarization of the t_{2g} orbitals. These two effects combine to modify the electronic band structure near the Fermi level and thus drive the system into an insulating state.

The analyses above show how the lattice degree of freedom affects the thermally driven magnetic/electronic transitions. Previous studies found that the Mott insulating state of 3% Ti-doped $Ca_3Ru_2O_7$ can be destroyed via non-thermal perturbations, e.g., by application of a modest magnetic field (~8 T) or low hydrostatic pressure (~0.04 GPa) [33,34]. Suppression of the insulating state by application of a magnetic field or pressure is accompanied by a structural transition from a short *c*-axis phase to a long *c*-axis phase. This remarkable feature indicates that the mechanism for the Mott transition that occurs on cooling in doped $Ca_3Ru_2O_7$ also applies to the Mott transition when tuned by application of non-thermal perturbations, such as magnetic fields, pressure and electronic fields.

IV. DEPENDENCE OF T_{MIT} ON STRUCTURAL FLATTENING ABOVE T_N

After disentangling the nature of Mott transition induced by thermal and non-thermal perturbations in Mn- and Ti-doped $Ca_3Ru_2O_7$, the question remains as to why these dramatic electronic and magnetic phase transitions can be induced by Ti and Mn doping but cannot be induced by Cr, Fe, Co, Ni and Cu doping. As discussed earlier, the Mott transitions that occur during temperature sweeps in Mn- and Ti-doped $Ca_3Ru_2O_7$ are associated with structural transitions. We therefore performed structural studies on samples with various dopants. Figure 4b shows that the compounds with the G-AFM Mott insulating state have smaller $c/\sqrt{ab}$ values than the compounds with the AFM-b localized states below T_N. More noticeably, this trend also extends to the PM metallic phase, which exists far above T_N. Figure 6 shows plots of the room temperature crystal structure parameters $c/\sqrt{ab}$ for the different compounds versus their MIT temperatures. Compounds with the G-AFM Mott insulating ground state are represented by the solid dots. Interestingly, we see that T_{MIT} is almost linearly dependent on the $c/\sqrt{ab}$ parameter, where a smaller value of $c/\sqrt{ab}$ results in a higher value of T_{MIT}. As indicated above, the G-AFM transition is accompanied by an abrupt reduction in $c/\sqrt{ab}$ at T_N/T_{MIT} (Fig. 4a), which appears to indicate that the structural flattening may be induced by the magnetic transition. If this was true, the role of 3*d* element doping would be that of tuning of the spin orders via magnetic interactions. However, the results that are shown in Fig. 6 do not support that conclusion. The Mott transition temperature is predetermined by the crystal structure in the high-temperature PM phase.

The compositions with the AFM-b ground states are represented by the hollow points in Fig. 6. These compositions are characterized by higher $c/\sqrt{ab}$ values than the samples that show the G-AFM ground state both below (Fig. 4b) and above T_N (Fig. 6). One direct implication of the above analysis is that we can probably predict whether the AFM Mott insulating state can occur or not based on the $c/\sqrt{ab}$ value at room temperature for any Ru-site-doped $Ca_3Ru_2O_7$ compound. Another implication is that the structural transitions drive the magnetic transitions, which provides a clue towards understanding of the simultaneous structural and magnetic transitions that occur in many correlated materials [42-44].

We can now summarize the realization of the Mott transition in doped $Ca_3Ru_2O_7$ in three steps. First, lattice flattening in the high-temperature PM metallic state is caused by Mn or Ti doping. Second, static tilting of the octahedron will result in a reduction of the *c*-axis on cooling. In a doped $Ca_3Ru_2O_7$ system, the $c/\sqrt{ab}$ values for each of the compositions decrease on cooling at a similar rate (approximately $-3\times10^{-3}/100$ K for the temperature-dependent lattice parameters of $Ca_3Ru_2O_7$ [28] and 9% Mn doping). Third, when $c/\sqrt{ab}$ reaches a critical value, the G-AFM state can be stabilized, as shown in Fig. 4b. A charge gap then opens as a result of the combined effects of the G-AFM stabilization and the orbital polarization via the LOC. The effects of the first two stages can lead to compensation, which is the reason for the linear dependence between the room temperature $c/\sqrt{ab}$ values and T_{MIT}. For example, the value of $c/\sqrt{ab}$ for a 10% Ti-doped sample at room temperature (3.5858) is smaller than that for the 9% Mn-doped sample (3.5931). This difference is equal to a cooling effect of ~67 K. Experimentally, the T_{MIT} of the 10% Ti-doped sample is ~60 K higher than that of the 9% Mn-doped sample.

As shown above, doping of ruthenates with Ti and Mn causes much stronger lattice distortions in the high-temperature metallic phase than doping with other 3*d* dopants. This nonmonotonic behavior cannot simply be explained by the variations of the ionic radii. Thus, the varied doping effects may be related to the different electronic configurations of dopants. We performed X-ray absorption near edge structure (XANES) spectrum measurements to investigate the valence states of these dopants (see Fig. 7). In Mn-doped $Ca_3Ru_2O_7$, we found that the XANES spectrum shifted from 6555.514 eV for 3% Mn doping to 6556.037 eV for 9% Mn doping, which indicated a valence change from Mn^{3+} for the lower doping concentration to Mn^{4+} for the higher doping concentration. This trend was also observed in Mn-doped Sr_2RuO_4 [45]. XANES spectrum measurements were also performed on Fe-doped $Ca_3Ru_2O_7$, with Fe_2O_3 powder crystal being used as a reference. Obviously, the absorption edges of the 3% Fe- and 5% Fe-doped samples were at higher energies (7129.498 eV and 7129.522 eV, respectively) than that of Fe_2O_3 (7124.004 eV), which indicated a valence that was higher than +3. Therefore, the outermost electronic states of the Mn and Fe dopants are Mn^{4+} (d^3) and Fe^{4+} (d^4), respectively.

It may be found that Ti^{4+} has fully empty 3*d* orbitals, and Mn^{4+} has fully empty spin-down t_{2g} orbitals and fully occupied spin-up t_{2g} orbitals. In the two cases, 3*d* states are all pushed away from the Fermi level. The undoped $Ca_3Ru_2O_7$ is metallic at room temperature, and Ru-4*d* states appear around the Fermi level. The mismatched *d*-orbital energies cause the bulk metallic state to be strongly scattered by Ti or Mn defects, leading to the strong structure distortions. On the other hand, Fe^{4+} have partly occupied *d*-orbitals appearing around the Fermi level, and thus the induced scattering is much weaker.

V. 3*d* DOPANTS IN TMOs: d^0/d^3 RULE

We analyzed some experimental data in other 3*d*-metal-doped oxides, and realized that the above dopant-scattering picture may be universal in correlated systems. Considering a transition metal oxide constructed using units of MO_6 octahedrons, if the M ion has a d^1, d^2, d^4 or d^5 configuration, the system should be metallic because the degenerate t_{2g} orbitals are partly occupied. However, we know that there are many d^1, d^2, d^4 or d^5 Mott insulators. Those Mott phases surely require specific structural distortions to lift the t_{2g} orbital degeneracy. In undoped systems, the structural distortion may be induced by a magnetic transition as temperature decreases. At high temperature, these systems are metallic.

When a 3*d*-dopant is introduced into these systems, there are two possible outcomes. If the *d* orbitals of the dopant are pushed away from the Fermi level, the dopant could then become a strong scattering center for the *d*-wave current of the high-temperature metallic phase. Therefore, **the low-temperature Mott phase is enhanced or a new competing insulating phase is induced**. Because the *3d*-orbital is highly localized, the strong scattering center is very likely to have a $3d^0$ or $3d^3$ configuration. The mechanism is illustrated in Fig. 8. Each Mn^{4+} ion carries three 3*d* electrons occupying the t_{2g} spin-up subband according to intra-atomic Hund's rule. If another electron is put to the site occupied by a Mn^{4+} ion, this electron must occupy the next available state, *i.e.* the t_{2g} spin-down subband or the e_g spin-up subband which is above the Fermi level[46,47]. This process surely costs additional energy. For Ti-doped samples, if another electron is put to the site occupied by a Ti^{4+} ion, it must occupy the Ti t_{2g} subband, which is also above the Fermi level according to the DFT calculations[23], thus causing the energy to increase. Therefore, either Mn^{4+} ($3d^3$) or Ti^{4+}($3d^0$)-occupied site is reasonably expected to be a strong scattering center due to the presence of an effective repulsive-potential barrier. The effects of strong scattering centers ($3d^0$ or $3d^3$ impurities) in ruthenates have been experimentally observed via scanning tunneling microscope (STM) measurements, such as the Freidel-like oscillations in Ti-doped Sr_2RuO_4 [48] and the local density of states (LDOS) modulations and quasiparticle interference effects in lightly Ti-doped $Sr_3Ru_2O_7$ [49]. $3d^3$/$3d^0$ strong scattering centers modify the local electron cloud configuration, thus resulting in local structural distortion. The strain field leads the local structural distortion to extend to the whole structure[50]. This mechanism reasonably explains why we could observe remarkable structural change even though the doping concentration is low.

In contrast, if the *d* orbitals of the dopant appear on the Fermi level, the dopant forms a weak scattering center. The doping effects of these dopants mainly result from carrier injection, which may then weaken the low-temperature Mott phase. This accounts for the Fe-, Cr-, Co-, and Ni-doping effect in $Ca_3Ru_2O_7$.

Using the explanation above, we can then understand the phase diagrams of 3*d*-element-doped $Ca_3Ru_2O_7$ and other 3*d*-element-doped ruthenates. The ground states of Sr_2RuO_4 and $Sr_3Ru_2O_7$ are both metallic. By $Ti^{4+}(d^0)$ and $Mn^{4+}(d^3)$ doping, AFM Mott transitions are induced in Sr_2RuO_4 and $Sr_3Ru_2O_7$, respectively. The room temperature c/a is reduced ~0.32% by 10% Ti doping in Sr_2RuO_4 [18], ~0.33% by 10% Mn doping in Sr_2RuO_4 [45], and ~0.47% by 6% Mn doping in $Sr_3Ru_2O_7$ [51]. More significantly, the MIT temperatures of $Sr_2(Ru_{1-x}Ti_x)O_4$ and $Sr_3(Ru_{1-x}Mn_x)_2O_7$ also show linear dependences on their room temperature c/a values, as shown in Fig. 9 [18,51].

Such a picture of $3d^0/3d^3$ strong scattering centers also accounts for the metal-to-insulator transition induced by Cr/Al doping in the 3*d* system V_2O_3. V_2O_3 caused great research interest since 1969, when its unusual phase diagram was discovered [52,53]. This compound transforms from a high-temperature corundum-structured paramagnetic metallic phase into a low-temperature monoclinic antiferromagnetic insulating phase at $T_N \sim 150$ K. When doped with Ti^{3+} or Cr^{3+}ions, V_2O_3 exhibits very different properties [52,54]. Upon substitution of V^{3+} by Ti^{3+}, the Néel temperature decreases and the antiferromagnetic phase vanishes for Ti doping of more than 5%. In contrast, substitution of V^{3+} by Cr^{3+} causes the Néel temperature to increase and it reaches ~180 K for 1.8% Cr doping. For higher Cr concentrations, T_N remains constant and the transition is then to a paramagnetic insulating phase. V_2O_3 is composed of VO_6 octahedrons and is a d^2 system. Ti^{3+} and Cr^{3+} dopants in V_2O_3 have local d^1 and d^3 configurations, respectively. Based on our conclusions above, the complex phase diagram of V_2O_3 can be explained phenomenologically. The d^3 dopant Cr^{3+} enhances the AFM Mott phase and induces a competing paramagnetic insulating phase, while the d^1 dopant Ti^{3+} conversely weakens the AFM Mott phase. Interestingly, Al^{3+} doping was found to have a similar effect on V_2O_3 to that of Cr^{3+} doping [55]. If Al is regarded as a d^0 dopant, the experimental results are then consistent with our explanation. As shown in Table 1 below, 3% Cr or Al doping causes T_N to increase from ~ 150 K to ~ 187 K. According to our proposed explanation, the LOC-induced or enhanced Mott transition requires significant structural distortions. In $Ca_3Ru_2O_7$, Sr_2RuO_4, and $Sr_3Ru_2O_7$, the critical structural distortions are described using the parameter *c/a*. In the Mott transition of V_2O_3, the critical structural parameters were indicated to be the V-V bond length (face sharing octahedron) and the *c/a* parameter [56]. The Cr^{3+} and Al^{3+} dopants have large and similar influences on the structure, and the Ti^{3+} dopant has a much weaker influence, as shown in Table 1.

We further found this picture can be applied to 5*d* systems, for example, Sr_2IrO_4 is a well-known spin-orbital Mott insulator with a long-range canted AFM structure. With 10% Mn^{4+} ($3d^3$) dopants, a new long-range magnetic structure with insulating state emerge through a reordering of the spins from the basal plane to the *c*-axis, indicating that a new competing insulating phase is induced[57]. We also note that the picture may be applied to some nonoxides, $BaVS_3$ experience a MIT at ~ 70 K associate with a structural transition from orthorhombic to monoclinic. As few as 2% Ti^{4+} ($3d^0$) dopants increased this transition temperature to ~ 250 K, indicating that the low-temperature Mott insulating phase is enhanced[58,59].

The above discussion shows that the proposed picture can explain some unusual phenomena in doped Mott systems, even the microscopic mechanism is unknown. Conversely, the picture may also help us to understand the Mott physics of undoped systems. To detect the relationships between the Mott transition and lattice, orbital degrees of freedom, we can deliberately introduce specific 3*d* dopants, acting as strong scattering centers, to a given system, and then measure the resulting responses.

VI. CONCLUSIONS

In summary, we indicated that the G-AFM Mott transitions that occurred in $Ca_3Ru_2O_7$ as a result of Mn or Ti doping can be unified into a simple picture of lattice-orbital coupling. The MIT temperature is found to be predetermined by the critical structural parameter $c/\sqrt{ab}$ at room temperature. We disclosed that the induced Mott transition originates in the strong scattering centers formed by these dopants. This type of dopant-scattering picture is universal for correlated systems, and it will help us to understand some previously controversial phenomena. We believe that that our findings will open a new thought to understand or tailor the physical properties of TMOs.

APPENDIX: EXPERIMENTAL METHODS

The single crystals that were used in this study were grown by the floating-zone technique. All samples that were used in the experiments were tested via X-ray diffraction (XRD) measurements and were shown to be composed of pure bilayer phases. The success of the doping of 3*d* dopants into the single crystals was confirmed by energy-dispersive X-ray spectroscopy (EDS). The real compositions are generally consistent with the nominal compositions when the doping level is less than 5%. However, the real compositions are smaller than the nominal ones when the doping level is more than 5%. The resistivity of the samples were measured via the four-probe method and an adiabatic relaxation technique, respectively, in a physical property measurement system (PPMS, Quantum Design). The magnetization measurements were performed using a superconducting quantum interference device (SQUID, Quantum Design) magnetometer. The neutron scattering measurements were performed using the HB1A thermal neutron triple-axis spectrometers at Oak Ridge National Laboratory. The X-ray absorption data at the Mn and Fe *K*-edges were recorded at room temperature in transmission mode at beamline BL14W1 of the Shanghai Synchrotron Radiation Facility (SSRF), China. The structural studies were performed by various methods, including neutron scattering measurements and XRD measurements. Rietveld refinements performed using the General Structure Analysis System (GSAS) code were used to analyze the XRD data, which were then collected via a step mode on the diffractometer (Rigaku TTR III) using powdered single crystals for each composition. Single-crystal XRD analysis was carried out using a Rigaku Saturn 724^+ charge-coupled device (CCD) diffractometer. The single-crystal neutron measurements were performed using the HB1A thermal neutron triple-axis spectrometers at Oak Ridge National Laboratory. Details of the determination of the structural parameters, including the error bars, are stated in the Supplementary Material [60].

ACKNOWLEDGEMENTS

The work performed at Nanjing University was supported by the National Natural Science Foundation of China (NNSFC) (grant nos. 11304149, U1332205, 11274153, 11204124, and 51202108). The work performed at Tulane University was supported by the U.S. Department of Energy under EPSCOR grant no. DE-SC0012432, with additional support being provided by the Louisiana Board of Regents (support for crystal growth, magnetization and transport measurements). X. K. would like to acknowledge the start-up fund provided by Michigan State University. The work performed at the High Magnetic Field Laboratory of the Chinese Academy of Sciences was supported by the NNSFC (grant nos. 11574322 and U1532153). G. L. was also supported by the NNSFC (grant nos. 11204326 and 11474296). The authors would also like to thank beamline BL14W1 at the Shanghai Synchrotron Radiation Facility for providing the beam time.

[1] M. Imada, A. Fujimori, and Y. Tokura, *Metal-insulator transitions,*Rev Mod Phys **70**, 1039 (1998).

[2] C. C. Tsuei and J. R. Kirtley, *Pairing symmetry in cuprate superconductors,*Rev Mod Phys **72**, 969 (2000).

[3] A. Damascelli, Z. Hussain, and Z.-X. Shen, *Angle-resolved photoemission studies of the cuprate superconductors,*Rev Mod Phys **75**, 473 (2003).

[4] A. L. Patrick, *From high temperature superconductivity to quantum spin liquid: progress in strong correlation physics,*Rep Prog Phys **71**, 012501 (2008).

[5] J. M. D. Coey, M. Viret, and S. von Molnár, *Mixed-valence manganites,*Adv Phys **48**, 167 (1999).

[6] Y. Tokura and Y. Tomioka, *Colossal magnetoresistive manganites,*J Magn Magn Mater **200**, 1 (1999).

[7] E. Dagotto, T. Hotta, and A. Moreo, *Colossal magnetoresistant materials: the key role of phase separation,*Physics Reports **344**, 1 (2001).

[8] M. B. Salamon and M. Jaime, *The physics of manganites: Structure and transport,*Rev Mod Phys **73**, 583 (2001).

[9] Y. Maeno, H. Hashimoto, K. Yoshida, S. Nishizaki, T. Fujita, J. G. Bednorz, and F. Lichtenberg, *Superconductivity in a layered perovskite without copper,*Nature **372**, 532 (1994).

[10] K. Ishida, H. Mukuda, Y. Kitaoka, K. Asayama, Z. Q. Mao, Y. Mori, and Y. Maeno, *Spin-triplet superconductivity in* Sr_2RuO_4 *identified by 17O Knight shift,*Nature **396**, 658 (1998).

[11] S. A. Grigera *et al.*, *Magnetic Field-Tuned Quantum Criticality in the Metallic Ruthenate* $Sr_3Ru_2O_7$*,*Science **294**, 329 (2001).

[12] S. Nakatsuji, D. Hall, L. Balicas, Z. Fisk, K. Sugahara, M. Yoshioka, and Y. Maeno, *Heavy-Mass Fermi Liquid near a Ferromagnetic Instability in Layered Ruthenates,*Phys Rev Lett **90**, 137202 (2003).

[13] J. M. Longo, P. M. Raccah, and J. B. Goodenough, *Magnetic Properties of* $SrRuO_3$ *and* $CaRuO_3$*,*J Appl Phys **39**, 1327 (1968).

[14] S. Nakatsuji, S.-i. Ikeda, and Y. Maeno, Ca_2RuO_4*: New Mott Insulators of Layered Ruthenate,*J Phys Soc Jpn **66**, 1868 (1997).

[15] J. E. Ortmann, J. Y. Liu, J. Hu, M. Zhu, J. Peng, M. Matsuda, X. Ke, and Z. Q. Mao, *Competition Between Antiferromagnetism and Ferromagnetism in* Sr_2RuO_4 *Probed by Mn and Co Doping,*Sci. Rep. **3** (2013).

[16] D. Mesa, F. Ye, S. Chi, J. A. Fernandez-Baca, W. Tian, B. Hu, R. Jin, E. W. Plummer, and J. Zhang, *Single-bilayer E-type antiferromagnetism in Mn-substituted* $Sr_3Ru_2O_7$*: Neutron scattering study,*Phys Rev B **85**, 180410 (2012).

[17] R. Mathieu *et al.*, *Impurity-induced transition to a Mott insulator in* $Sr_3Ru_2O_7$*,*Phys Rev B **72**, 092404 (2005).

[18] K. Pucher *et al.*, *Transport, magnetic, thermodynamic, and optical properties in Ti-doped* Sr_2RuO_4*,*Phys Rev B **65**, 104523 (2002).

[19] M. Braden, O. Friedt, Y. Sidis, P. Bourges, M. Minakata, and Y. Maeno, *Incommensurate Magnetic Ordering in* $Sr_2Ru_{1-x}Ti_xO_4$*,*Phys Rev Lett **88**, 197002 (2002).

[20] J. P. Carlo *et al.*, *New magnetic phase diagram of* $(Sr,Ca)_2RuO_4$*,*Nat Mater **11**, 323 (2012).

[21] P. Steffens, J. Farrell, S. Price, A. P. Mackenzie, Y. Sidis, K. Schmalzl, and M. Braden, *Incommensurate magnetic ordering in Ti-doped* $Sr_3Ru_2O_7$*,*Phys Rev B **79**, 054422 (2009).

[22] J. Peng, X. Ke, G. Wang, J. E. Ortmann, D. Fobes, T. Hong, W. Tian, X. Wu, and Z. Q. Mao, *From quasi-two-dimensional metal with ferromagnetic bilayers to Mott insulator with G-type antiferromagnetic order in* $Ca_3(Ru_{1-x}Ti_x)_2O_7$*,*Phys Rev B **87**, 085125 (2013).

[23] X. Ke, J. Peng, D. J. Singh, T. Hong, W. Tian, C. R. Dela Cruz, and Z. Q. Mao, *Emergent electronic and magnetic state in* $Ca_3Ru_2O_7$ *induced by Ti doping,*Phys Rev B **84**, 201102 (2011).

[24] P. Li, A. Maignan, R. Retoux, and B. Raveau, *Substitution at the Ru site in the itinerant ferromagnet SrRuO 3,*J. Phys. Condens. Matter **14**, 7391 (2002).

[25] Z. H. Han, J. I. Budnick, W. A. Hines, B. Dabrowski, S. Kolesnik, and T. Maxwell, *Nuclear magnetic resonance study of the enhanced ferromagnetic ordering in polycrystalline* $SrRu_{1-x}Cr_xO_3$ $(0 \leqslant x \leqslant 0.12)$*,*Journal of Physics: Condensed Matter **17**, 1193 (2005).

[26] V. Durairaj, S. Chikara, X. N. Lin, A. Douglass, G. Cao, P. Schlottmann, E. S. Choi, and R. P. Guertin, *Highly anisotropic magnetism in Cr-doped perovskite ruthenates,*Phys Rev B **73**, 214414 (2006).

[27] G. Cao, S. McCall, J. E. Crow, and R. P. Guertin, *Observation of a Metallic Antiferromagnetic Phase and Metal to Nonmetal Transition in* $Ca_3Ru_2O_7$*,*Phys. Rev. Lett. **78**, 1751 (1997).

[28] Y. Yoshida, S.-I. Ikeda, H. Matsuhata, N. Shirakawa, C. H. Lee, and S. Katano, *Crystal and magnetic structure of* $Ca_3Ru_2O_7$*,*Phys Rev B **72**, 054412 (2005).

[29] W. Bao, Z. Q. Mao, Z. Qu, and J. W. Lynn, *Spin Valve Effect and Magnetoresistivity in Single Crystalline* $Ca_3Ru_2O_7$*,*Phys Rev Lett **100**, 247203 (2008).

[30] Y. Yoshida, I. Nagai, S.-I. Ikeda, N. Shirakawa, M. Kosaka, and N. Môri, *Quasi-two-dimensional metallic ground state of*$Ca_3Ru_2O_7$*,*Physical Review B **69**, 220411 (2004).

[31] F. Baumberger *et al.*, *Nested Fermi Surface and Electronic Instability in* $Ca_3Ru_2O_7$*,*Phys Rev Lett **96**, 107601 (2006).

[32] G.-Q. Liu, *Mott transition and magnetic anisotropy in* $Ca_3Ru_2O_7$*,*Phys Rev B **84**, 235137 (2011).

[33] M. Zhu, J. Peng, T. Zou, K. Prokes, S. D. Mahanti, T. Hong, Z. Q. Mao, G. Q. Liu, and X. Ke, *Colossal Magnetoresistance in a Mott Insulator via Magnetic Field-Driven Insulator-Metal Transition,*Phys Rev Lett **116**, 216401 (2016).

[34] T. Zou *et al.*, *Pressure-induced electronic and magnetic phase transitions in a Mott insulator: Ti-doped* $Ca_3Ru_2O_7$ *bilayer ruthenate,*Physical Review B **94**, 041115 (2016).

[35] S. N. Ruddlesden and P. Popper, *The compound Sr3Ti2O7 and its structure,*Acta Crystallographica **11**, 54 (1958).

[36] X. Ke, J. Peng, W. Tian, T. Hong, M. Zhu, and Z. Q. Mao, *Commensurate-incommensurate magnetic phase transition in the Fe-doped bilayer ruthenate* $Ca_3Ru_2O_7$*,*Physical Review B **89**, 220407 (2014).

[37] See supplemental material at for temperature dependent magnetic susceptibilities and heat capacity of 2% Mn and 2% Fe doped sample

[38] G. Cao, V. Durairaj, S. Chikara, L. E. DeLong, and P. Schlottmann, *Observation of Strong Spin Valve Effect in Bulk* $Ca_3(Ru_{1-x}Cr_x)_2O_7$*,*Phys Rev Lett **100**, 016604 (2008).

[39] O. Friedt, M. Braden, G. André, P. Adelmann, S. Nakatsuji, and Y. Maeno, *Structural and magnetic aspects of the metal-insulator transition in* $Ca_{2-x}Sr_xRuO_4$*,*Phys Rev B **63**, 174432 (2001).

[40] Z. Fang, N. Nagaosa, and K. Terakura, *Orbital-dependent phase control in* $Ca_{2-x}Sr_xRuO_4$ *(0<~x<~0.5),*Physical Review B **69**, 045116 (2004).

[41] J. H. Jung, Z. Fang, J. P. He, Y. Kaneko, Y. Okimoto, and Y. Tokura, *Change of Electronic Structure in* Ca_2RuO_4 *Induced by Orbital Ordering,*Phys Rev Lett **91**, 056403 (2003).

[42] P. G. Radaelli, D. E. Cox, M. Marezio, S. W. Cheong, P. E. Schiffer, and A. P. Ramirez, *Simultaneous Structural, Magnetic, and Electronic Transitions in* $La_{1-x}Ca_xMnO_3$ *with x=0.25 and 0.50,*Phys Rev Lett **75**, 4488 (1995).

[43] S. Li *et al.*, *First-order magnetic and structural phase transitions in* $Fe_{1+y}Se_xTe_{1-x}$*,*Phys Rev B **79**, 054503 (2009).

[44] Q. Huang, Y. Qiu, W. Bao, M. A. Green, J. W. Lynn, Y. C. Gasparovic, T. Wu, G. Wu, and X. H. Chen, *Neutron-Diffraction Measurements of Magnetic Order and a Structural Transition in the Parent* $BaFe_2As_2$ *Compound of FeAs-Based High-Temperature Superconductors,*Phys Rev Lett **101**, 257003 (2008).

[45] L. Zheng, J. Cai, Q. Xie, B. Lv, Z. Q. Mao, and X. S. Wu, *Mn induced ferromagnetism spin fluctuation enhancement in* $Sr_2Ru_{1-x}Mn_xO_4$*,*J Magn Magn Mater **342**, 115 (2013).

[46] W. A. Harrison, *Elementary Electronic Structure (revised Edition),*Environmental Earth Sciences (2004).

[47] See Supplementary Material for details of enegy levels of Ru and Mn *d* orbitals. .

[48] B. I. Barker, S. K. Dutta, C. Lupien, P. L. McEuen, N. Kikugawa, Y. Maeno, and J. C. Davis, *STM studies of individual Ti impurity atoms in* Sr_2RuO_4*,*Physica B: Condensed Matter **329–333, Part 2**, 1334 (2003).

[49] J. Lee, M. P. Allan, M. A. Wang, J. Farrell, S. A. Grigera, F. Baumberger, J. C. Davis, and A. P. Mackenzie, *Heavy d-electron quasiparticle interference and real-space electronic structure of* $Sr_3Ru_2O_7$*,*Nat Phys **5**, 800 (2009).

[50] A. I. Frenkel, D. M. Pease, J. I. Budnick, P. Metcalf, E. A. Stern, P. Shanthakumar, and T. Huang, *Strain-Induced Bond Buckling and Its Role in Insulating Properties of Cr-Doped* V_2O_3*,*Phys Rev Lett **97**, 195502 (2006).

[51] B. Hu, G. T. McCandless, V. O. Garlea, S. Stadler, Y. Xiong, J. Y. Chan, E. W. Plummer, and R. Jin, *Structure-property coupling in* $Sr_3(Ru_{1-x}Mn_x)_2O_7$*,*Phys Rev B **84**, 174411 (2011).

[52] D. B. McWhan, A. Menth, J. P. Remeika, W. F. Brinkman, and T. M. Rice, *Metal-Insulator Transitions in Pure and Doped* V_2O_3*,*Phys Rev B **7**, 1920 (1973).

[53] D. B. McWhan and J. P. Remeika, *Metal-Insulator Transition in* $(V_{1-x}Cr_x)_2O_3$*,*Phys Rev B **2**, 3734 (1970).

[54] S. Chen, J. E. Hahn, C. E. Rice, and W. R. Robinson, *The effects of titanium or chromium doping on the crystal structure of* V_2O_3*,*J Solid State Chem **44**, 192 (1982).

[55] H. V. K. G. M. Joshi, H. Kuwamoto, J. M. Honig, *Structure & Properties of Cr- & Al-doped* V_2O_3 *- A Comparison,*Indian Journal of Pure & Applied Physics **15**, 471 (1977).

[56] P. D. Dernier and M. Marezio, *Crystal Structure of the Low-Temperature Antiferromagnetic Phase of* V_2O_3*,*Phys Rev B **2**, 3771 (1970).

[57] S. Calder, G. X. Cao, M. D. Lumsden, J. W. Kim, Z. Gai, B. C. Sales, D. Mandrus, and A. D. Christianson, *Magnetic structural change of* Sr_2IrO_4 *upon Mn doping,*Phys Rev B **86**, 220403 (2012).

[58] T. Learmonth, P. A. Glans, J. H. Guo, M. Greenblatt, and K. E. Smith, *Electronic excitations in the correlated metal* $BaV_{0.98}Ti_{0.02}S_3$ *studied using resonant inelastic soft x-ray scattering,*Journal of Physics: Condensed Matter **22**, 025504 (2010).

[59] S. Fagot, P. Foury-Leylekian, J.-P. Pouget, G. Popov, M. Lobanov, M. Greenblatt, and P. Fertey, *Structural instabilities in Nb, Ti and K substituted* $BaVS_3$*,*Physica B: Condensed Matter **378**, 1068 (2006).

[60] See Supplementary Material at for details of XRD measurements and Rietveldt refinements.

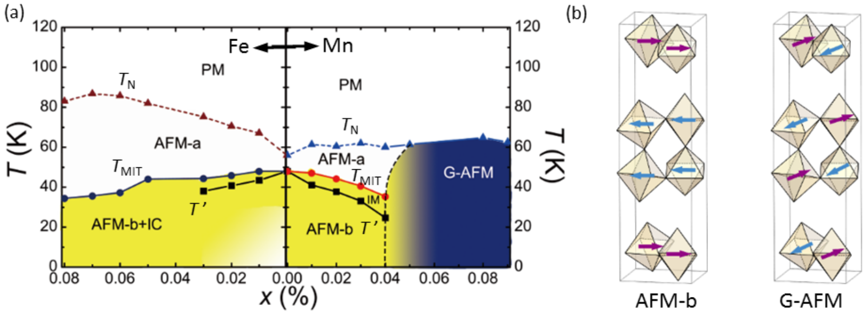

FIG. 1. (a) Magnetic and electronic phase diagrams of $Ca_3(Ru_{1-x}Mn_x)_2O_7$ and $Ca_3(Ru_{1-x}Fe_x)_2O_7$, where IM represents the intermediate magnetic state; boundaries among the various magnetic states are indicated by solid/dashed lines. Metallic (white), localized (yellow) and insulating (blue) electronic states are represented by the different colored zones. (b) Schematic diagrams of the magnetic structures AFM-b and G-AFM.

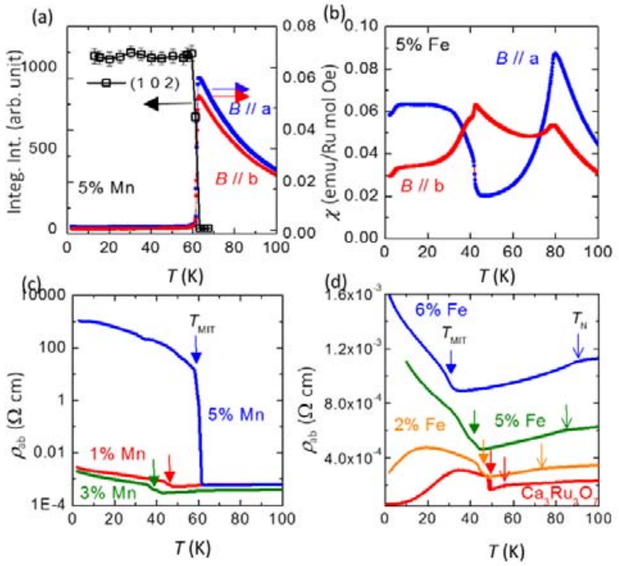

FIG. 2. (a) Temperature dependence of magnetic susceptibility under a 5000 Oe magnetic field for Ca$_3$(Ru$_{0.95}$Mn$_{0.05}$)$_2$O$_7$. The integrated intensity of the magnetic Bragg reflections was measured via neutron diffraction at (1 0 2) for Ca$_3$(Ru$_{0.95}$Mn$_{0.05}$)$_2$O$_7$. (b) Temperature dependence of magnetic susceptibility under a 5000 Oe magnetic field that was applied along both the *a*- and *b*-axes for Ca$_3$(Ru$_{0.95}$Fe$_{0.05}$)$_2$O$_7$. (c) In-plane resistivity of Ca$_3$(Ru$_{1-x}$Mn$_x$)$_2$O$_7$ (where x = 0.01, 0.03 and 0.05). (d) values of Ca$_3$Ru$_2$O$_7$ and Ca$_3$(Ru$_{1-x}$Fe$_x$)$_2$O$_7$ (where x = 0.02, 0.05 and 0.06). A monotonic increase in T_N and monotonic reduction of T_{MIT} are both clearly observed.

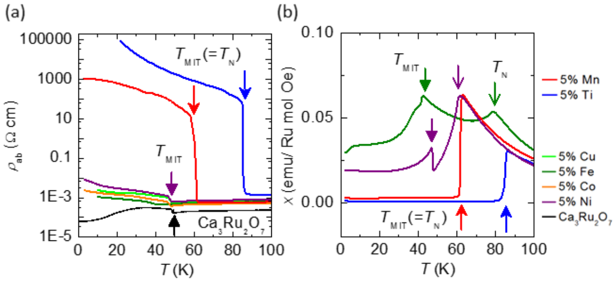

FIG. 3. (a) ρ_{ab} characteristics of $Ca_3Ru_2O_7$ and 5% Cu-, Fe-, Co-, Ni-, Mn- and Ti-doped $Ca_3Ru_2O_7$ samples. (b) Temperature dependences of magnetic susceptibilities under a 5000 Oe magnetic field along the *a*-axes of the 5% Fe-, Ni-, Mn- and Ti-doped $Ca_3Ru_2O_7$ samples.

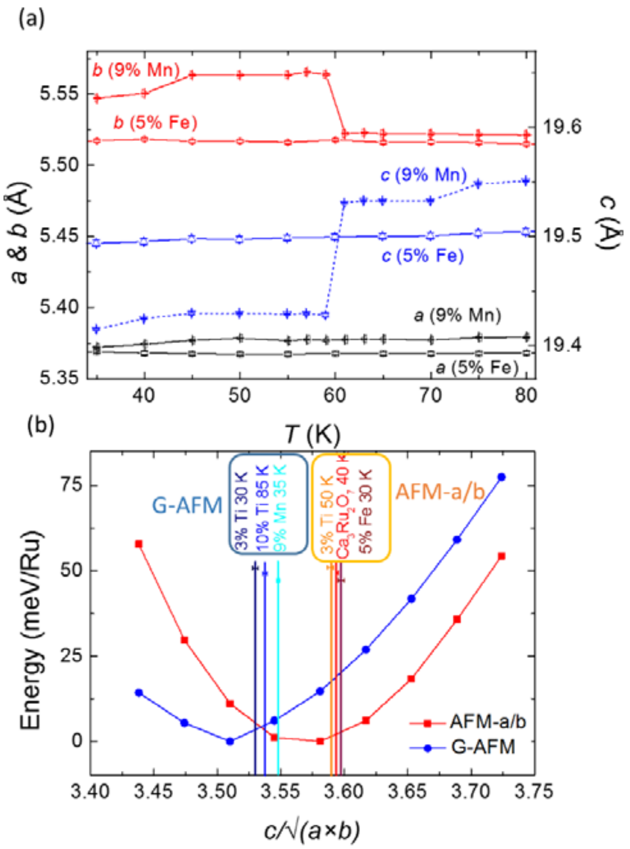

FIG. 4. (a) Lattice parameters *a*, *b* and *c* of $Ca_3(Ru_{0.91}Mn_{0.09})_2O_7$ and $Ca_3(Ru_{0.95}Fe_{0.05})_2O_7$ versus temperature. (b) Dependence of the total energy on the structural parameter $c/\sqrt{ab}$ for the AFM-a/b and G-AFM magnetic states, as obtained via DFT calculations. Vertical lines indicate the $c/\sqrt{ab}$ parameters that were derived from experimental data for $Ca_3Ru_2O_7$ at 40 K [28], 3% Ti doping at 50 K [23], 5% Fe doping at 30 K, 9% Mn doping at 35 K, 10% Ti doping at 90 K and 3% Ti doping at 30 K [23].

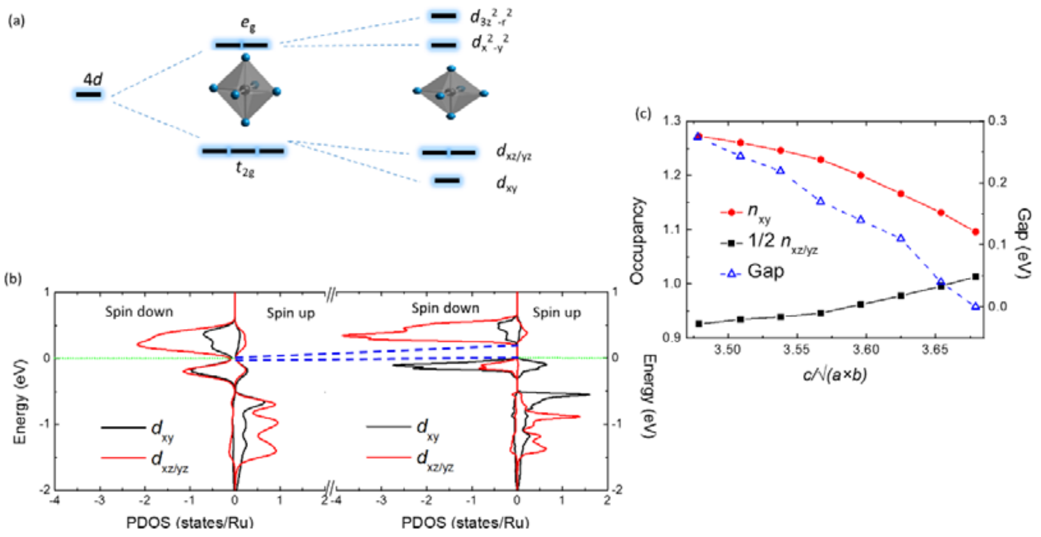

FIG. 5. (a) Schematic diagram showing energy levels of 4*d* orbital for two states with undistorted and flattened octahedrons. (b) Calculated PDOS of the t_{2g} orbitals of Ru for normal and small $c/\sqrt{ab}$ ratios. (c) Calculated d_{xy} and $d_{xz/yz}$ orbital occupancy numbers and band gap values as a function of the structural parameter $c/\sqrt{ab}$.

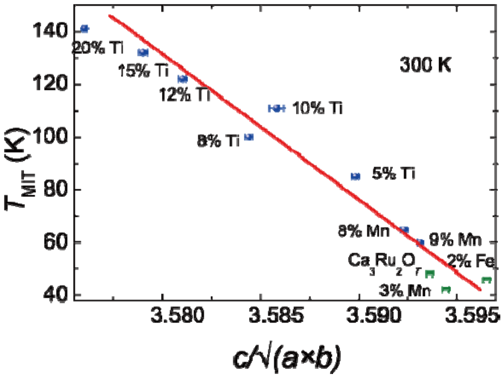

FIG. 6. Relationship between T_{MIT} and $c/\sqrt{ab}$ at 300 K for materials with the G-AFM insulating ground state (9% Mn-, 8% Mn-, 5% Ti- , 8% Ti-, 10% Ti-, 15% Ti-, 20% Ti-doped samples [22]) and for materials with AFM-b localized or metallic ground states (3% Mn- and 2% Fe-doped samples and $Ca_3Ru_2O_7$ [28]).

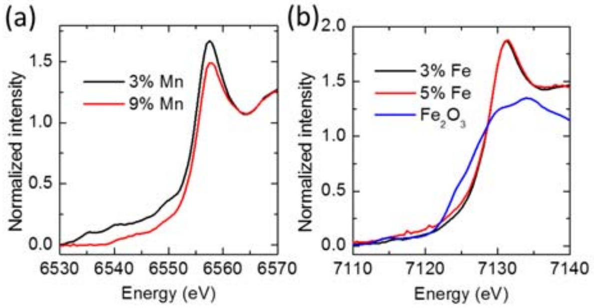

FIG. 7. (a) Normalized XAFS spectra of the Mn-*K* edges of 3% and 9% Mn-doped $Ca_3Ru_2O_7$. (b) Normalized XAFS spectra of the Fe-*K* edges of 3% and 5% Fe-doped $Ca_3Ru_2O_7$ and Fe_2O_3.

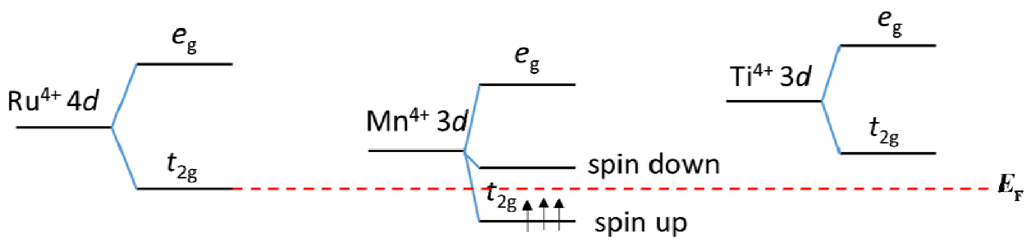

FIG. 8: The relative crystal-field-split energy levels of Ru, Mn and Ti ions for $Ca_3(Ru_{1-x}M_x)_2O_7$ (M = Mn or Ti) system[46].

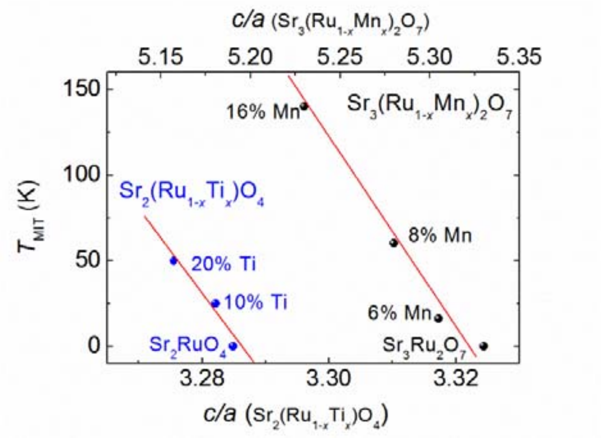

FIG. 9. Relationships between T_{MIT} and c/a at 300 K for $Sr_2(Ru_{1-x}Ti_x)O_4$ and $Sr_3(Ru_{1-x}Mn_x)_2O_7$ [18,51].

	Dopant configuration	T_N	V-V(face shared) (300K)	c/a (300K)
V_2O_3		~ 150 K	~2.700	~2.828
~3% Cr	d^3	~ 187 K	~2.748	~2.785
~3% Al	d^0	~ 187 K	Not reported	~2.78
~3% Ti	d^1	~ 100 K	~2.706	~2.82

Table 1. Magnetic transition temperature and room temperature structural parameters for V_2O_3 and Cr-, Al- and Ti-doped V_2O_3 [54,55].